Supplementary Information : Signature of a randomness-driven spin-liquid state in a frustrated magnet

J. Khatua,[1] M. Gomilšek,[2,3] J. C. Orain,[4] A. M. Strydom,[5,6] Z. Jagličić,[7,8] C. V. Colin,[9] S. Petit,[10] A. Ozarowski,[11] L. Mangin-Thro,[12] K. Sethupathi,[1,13] M.S. Ramachandra Rao,[13,14] A. Zorko,[2,3] and P. Khuntia *[1,13,15]

[1]*Department of Physics, Indian Institute of Technology Madras, Chennai 600036, India*

[2]*Jožef Stefan Institute, Jamova c. 39, 1000 Ljubljana, Slovenia*

[3]*Faculty of Mathematics and Physics, University of Ljubljana, Jadranska u. 19, 1000 Ljubljana, Slovenia*

[4]*Paul Scherrer Institute, Bulk MUSR group, LMU 5232 Villigen PSI, Switzerland*

[5]*Highly Correlated Matter Research Group, Department of Physics, University of Johannesburg, PO Box 524, Auckland Park 2006, South Africa*

[6]*Max Planck Institute for Chemical Physics of Solids, 40 Nöthnitzerstr., Dresden D-01187, Germany.*

[7]*Faculty of Civil and Geodetic Engineering, University of Ljubljana, 1000 Ljubljana, Slovenia*

[8]*Institute of Mathematics, Physics and Mechanics, 1000 Ljubljana, Slovenia*

[9]*Institut Néel, Université Grenoble Alpes, CNRS, Grenoble, 38042, France*

[10]*LLB, CEA, CNRS, Université Paris-Saclay, CEA Saclay, 91191 Gif-sur-Yvette, France*

[11]*National High Magnetic Field Laboratory, Florida State University, Tallahassee, Florida 32310, USA*

[12]*Institut Laue-Langevin, 38042 Grenoble, France*

[13]*Quantum Centre for Diamond and Emergent Materials, Indian Institute of Technology Madras, Chennai 600036, India.*

[14]*Department of Physics, Nano Functional Materials Technology Centre and Materials Science Research Centre,*

Indian Institute of Technology Madras, Chennai-600036, India

[15]*Functional Oxide Research Group,*

Indian Institute of Technology Madras, Chennai 600036, India.

Supplementary Note 1 : Powder X-ray diffraction of Li_4CuTeO_6

The Rietveld refinement of XRD data (Supplementary Figure 1) was performed to check sample purity and determine the lattice parameters. The obtained lattice parameters of LCTO are consistent with the estimated lattice parameters from neutron diffraction data as summarized in Supplementary Table I.

Supplementary Note 2 : Neutron diffraction of Li_4CuTeO_6

Due to light mass of Li and O atoms, the analysis of X-ray powder diffraction data is not sufficient to determine the structural disorder and mixed site occupancy. Therefore, neutron diffraction measurements were performed on crg-D1B two-axis diffractometer at the ILL at room temperature at 1.28 Å. The refined crystallographic structure is tabulated in Supplementary Table I.

Supplementary Table I: Refined atomic parameters for LCTO determined by neutron diffraction at 300 K with a space group $C2/m$ (No. 12) for the incident wavelength 1.28 Å. The obtained monoclinic lattice constants are $a = 5.2752(5)$ Å, $b = 8.8163(8)$ Å , $c = 5.2457(5)$ Å and $\beta = 113.172(8)$ Å, $\alpha = \gamma = 90.0^0$, Vol = 224.28(4) Å^3 and $R_{Bragg} = 1.74$.

Atom	Wyckoff position	x	y	z	Occ.
Te_1	$2a$	0.00000	0.00000	0.00000	1
Li_1	$4h$	0.00000	0.1676(6)	0.50000	1
Li_2	$2d$	0.50000	0.00000	0.50000	0.161(3)
Cu_2	$2d$	0.50000	0.00000	0.50000	0.839(3)
Li_3	$4g$	0.00000	0.3421(9)	0.00000	0.934(2)
Cu_3	$4g$	0.00000	0.3421(9)	0.00000	0.066(2)
O_1	$4i$	0.2196(4)	0.00000	0.7861(4)	1
O_2	$8j$	0.2406(3)	0.15131(9)	0.2464(3)	1

∗. pkhuntia@iitm.ac.in

Supplementary Note 3 : Magnetization and ac susceptibility

Supplementary Figure 2 shows the magnetization isotherms at several temperatures that were used to demonstrate data collapse behaviour in the main manuscript (Fig. 2 (d)). In addition to ac susceptibility measurement in the temperature range 0.045 K $\leq T \leq$ 4 K (Fig. 2 (c) in main text), we also performed ac susceptibility measurement in the temperature range 2 K $\leq T \leq$ 50 K at different frequencies as shown in Supplementary Figure 3. The absence of frequency dependence of the the real part of ac susceptibility suggests the absence of spin glass transition in Li_4CuTeO_6.

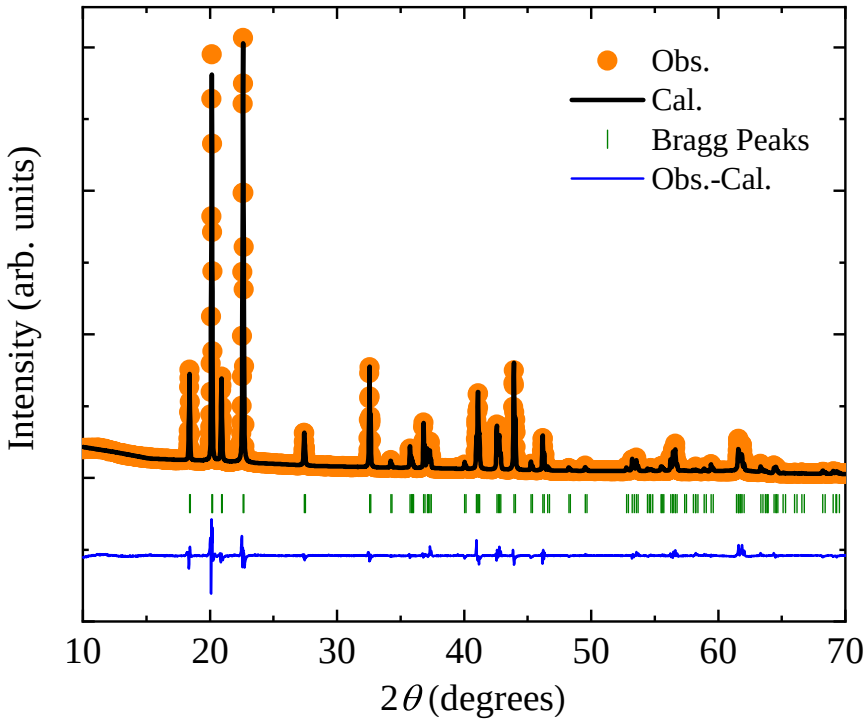

Supplementary Figure 1: Rietveld refinement of X-ray diffraction data of LCTO at room temperature. The solid circles represent the observed intensity (Obs.) whereas the black solid line is the calculated intensity (cal.). The olive vertical bars represent the Bragg reflection positions and the residual data are denoted by the blue solid line that is shifted vertically for clarity.

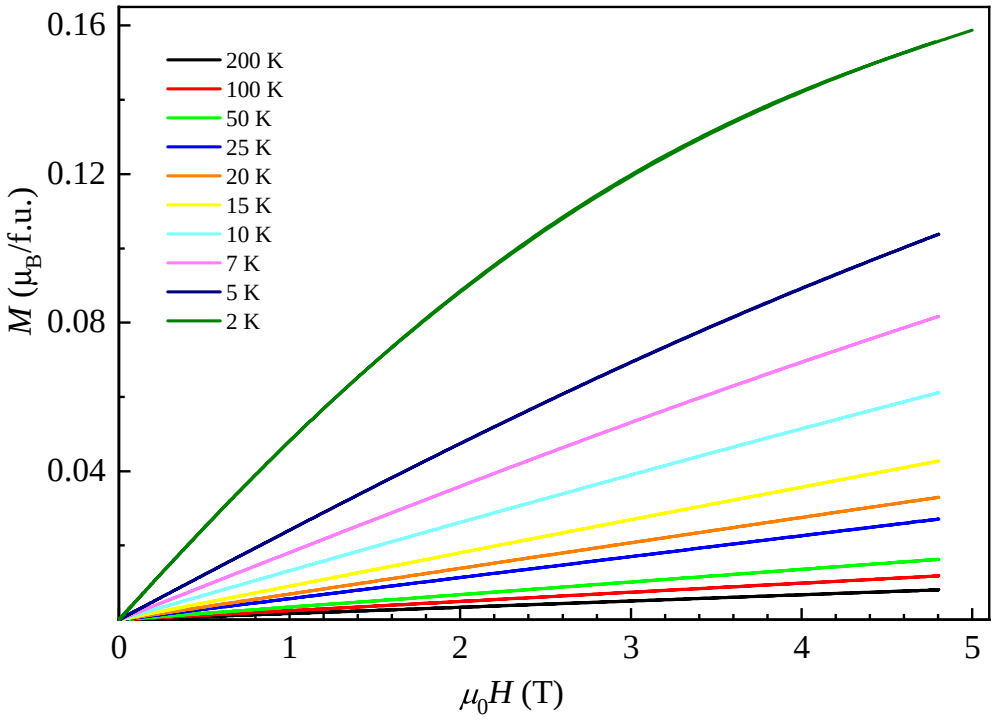

Supplementary Figure 2: Magnetization isotherm at multiple temperatures.

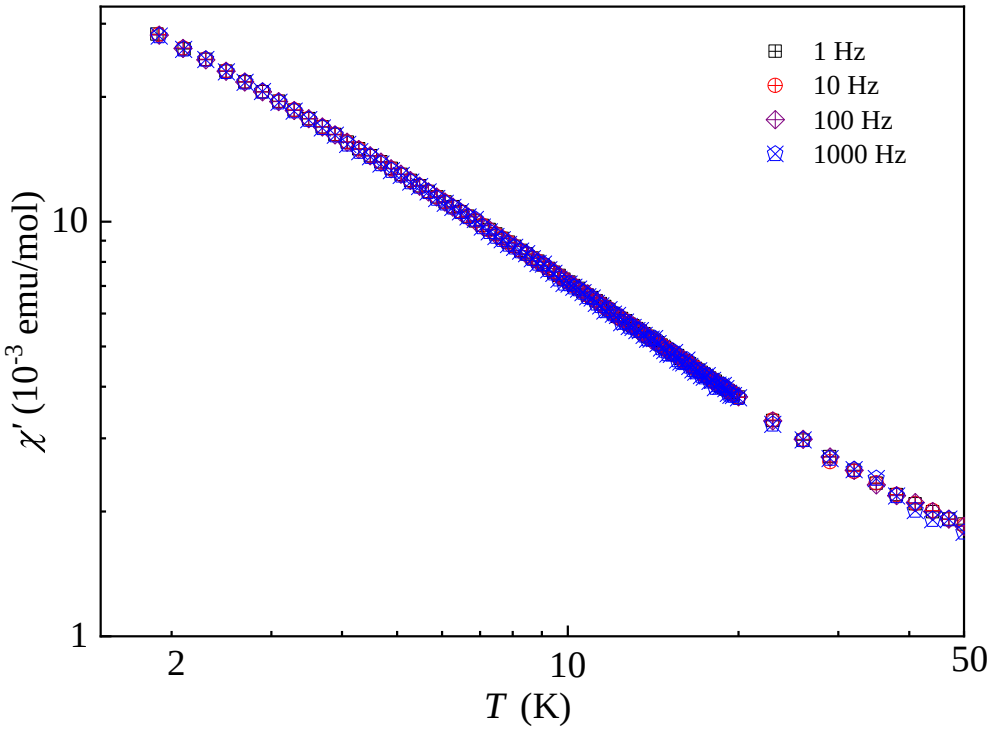

Supplementary Figure 3: Temperature dependence of real part of ac susceptibility at different frequencies in the temperature range 2 K $\leq T \leq$ 50 K.

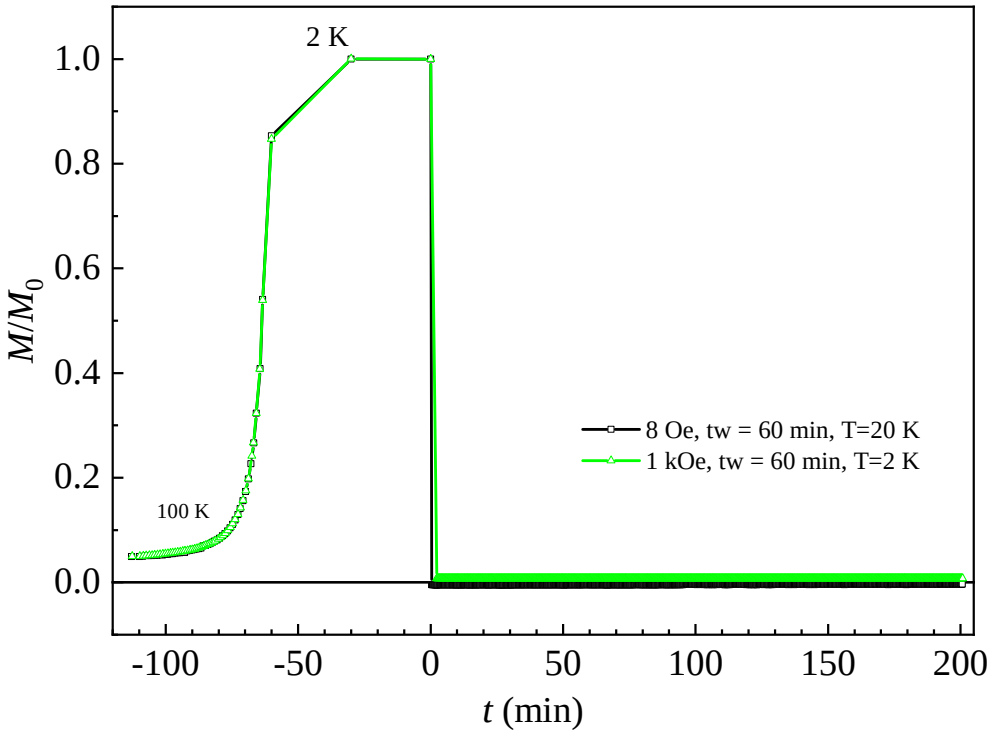

Supplementary Figure 4: Normalized isotherm magnetization as a function of time in different fields where M_0 is a magnetization at 2 K and corresponding magnetic field of 8 or 1000 Oe just before it is turned off.

Supplementary Note 4 : Thermoremnant magnetization

In order to confirm the absence of spin-glass behaviour, the sample was cooled down from 100 to 2 K in either 1000 or 8 Oe. After 1h, the field was turned down and the signal was measured again (at $t = 0$). The signal is practically zero (in 1 kOe a small signal is still observed which is due to the remnant field of the superconducting magnet) and does not decay with time (Supplementary Figure 4). This indicates there is no sign of a spin-glass transition in Li_4CuTeO_6.

Supplementary Note 5 : Specific heat

Supplementary Figure 5 depicts the specific heat data in zero field down to 52 mK which suggests the absence of magnetic ordering in Li_4CuTeO_6 despite strong antiferromagnetic interaction between Cu^{2+} moments. In order to gain further insights into the magnetic properties relevant to this frustrated magnet and understand the ground-state degeneracy, it

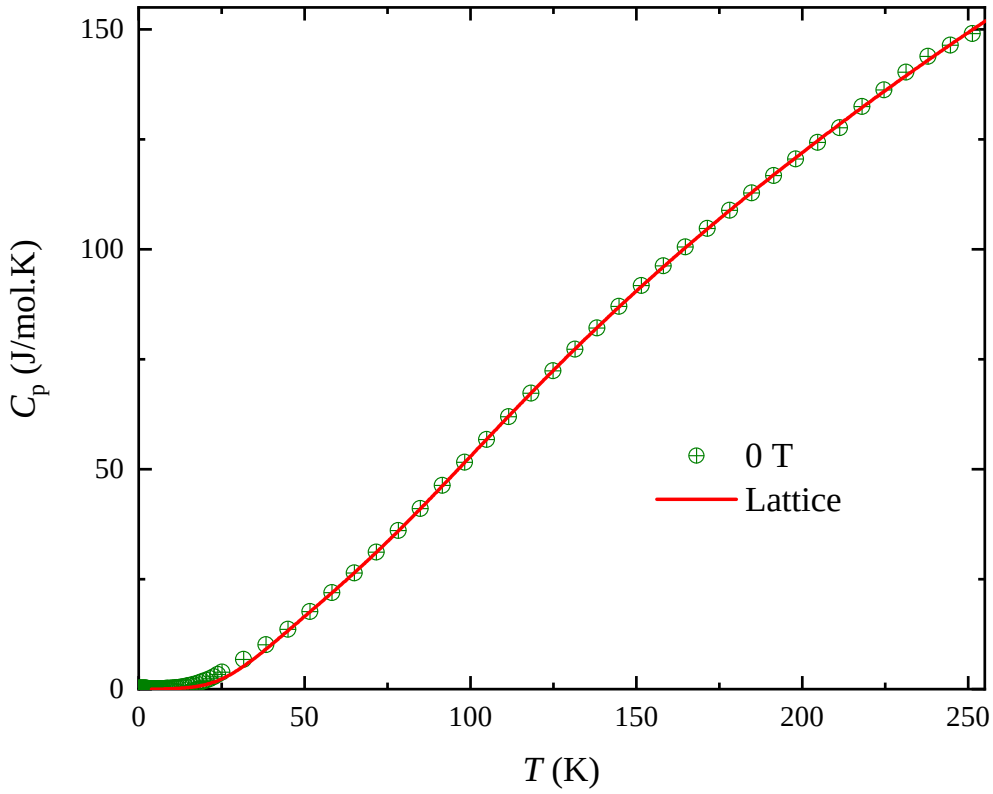

Supplementary Figure 5: Temperature dependence of the specific heat (C_p) in zero magnetic field down to 52 mK, where the red line is the lattice contribution to the specific heat above 20 K taking into account Debye and Einstein models (Eq. 1).

is important to extract magnetic specific heat. We have considered the zero-field specific heat data (C_p) as a sum of magnetic specific heat ($C_{\rm mag}$) due to Cu^{2+} ions and lattice specific heat ($C_{\rm lattice}$) due to phonons. In the absence of a suitable iso-structural non-magnetic analogue of Li_4CuTeO_6, we have considered the following function for the lattice heat capacity,

$$C_{\rm lattice}(T) = C_D[9k_B\left(\frac{T}{\theta_D}\right)^3\int_0^{\theta_D/T}\frac{x^4e^x}{(e^x-1)^2}dx] \; + \\ \sum_{i=1}^{3}C_{E_i}[3R\left(\frac{\theta_i}{T}\right)^2\frac{\exp(\frac{\theta_{\rm E_i}}{T})}{(\exp(\frac{\theta_{\rm E_i}}{T})-1)^2}], \qquad (1)$$

which includes one Debye term and three Einstein terms. In the first term of Eq. (1) fitting parameter θ_D is the Debye temperature and in the second term Einstein temperatures θ_i are the fitting parameter and R and k_B are the molar gas constant and Boltzmann constant respectively. As depicted in Supplementary Figure 5, the experimental data show good agreement with the model lattice contribution (solid red line) with one Debye and three Einstein

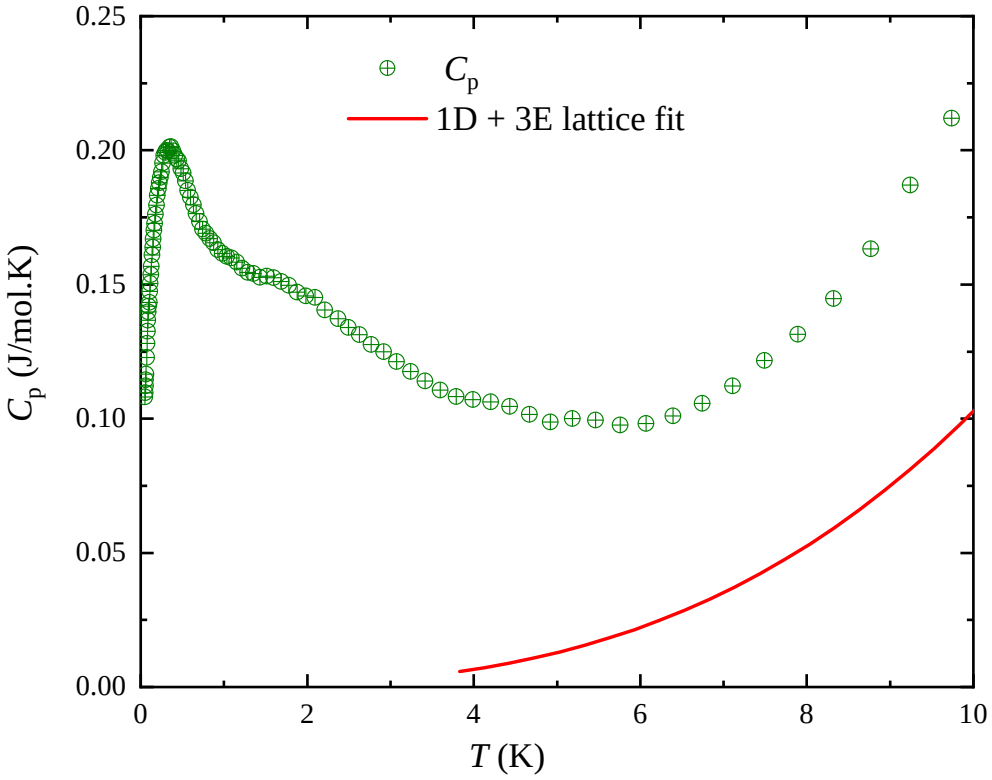

Supplementary Figure 6: The temperature dependence of the specific heat (C_p) in zero magnetic field in the temperature range 52 mK $\leq T \leq$ 10 K, where the red line is the lattice contribution to the specific heat above 20 K taking into account Debye and Einstein models (Eq. 1).

terms in the temperature range 30 K $\leq T \leq$ 120 K. Here the coefficients of the Debye term C_D and Einstein terms C_{E_1}, C_{E_2} and C_{E_3} terms are the relative weights of acoustic vibrational mode and optical vibrational modes. The best fit, shown in Supplementary Figure 5 is obtained for $\theta_D = 191$ K, $\theta_{E_1} = 323$ K, $\theta_{E_2} = 586$ K, and $\theta_{E_3} = 960$ K, while the coefficients were fixed in the ratio $C_d : C_{E_1} : C_{E_2} : C_{E_3} = 1 : 2 : 4 : 5$ to minimized the fit parameters. Since there are twelve atoms in one formula unit of LCTO, the sum of these coefficient is equivalent with the sum of the ratio of number of acoustic modes (3) to the number of optical modes (33). It is observed that the Debye-Einstein model fit very well (red line in Supplementary Figure 5) to the C_p data above 30 K but it fails to account for data below 30 K (Supplementary Figure 6)) [1]. Therefore, specific heat data below 30 K were fitted with βT^3 to extract magnetic specific heat in different fields.

Supplementary Note 6 : *Ab initio* DFT+U exchange calculations

Exchange couplings in Li_4CuTeO_6 were calculated using the CASTEP plane-wave *ab initio* density functional theory (DFT) code [2] with ultrasoft pseudopotentials under the local (spin) density approximation (LSDA) exchange-correlation functional with additional Hubbard repulsion in an LSDA+U scheme [3]. An effective on-site Hubbard repulsion of $U_{\rm eff} = U - J_H = 9\,$meV, where $U = 10\,$meV is the bare Hubbard repulsion and $J_H = 1\,$meV is Hund's coupling, was chosen throughout, consistently with previous LSDA+U results on the related Cu_3TeO_6 compound [4]. Calculations were carried out on a DFT geometry-optimized $2\times1\times2$ supercell to capture exchange interactions between further-away Cu^{2+}, with a 2000 eV plane-wave energy cutoff and a $2\times3\times2$ Monkhorst-Pack grid reciprocal-space sampling [5] to achieve numerical convergence. Isotropic (Heisenberg) exchange couplings were extracted within the total-energy (broken-symmetry) DFT framework [6] by calculating total DFT energies of $\geq$120 random collinear spin configurations with spins pointing along the crystallographic c axis. We note that the LSDA+U scheme systematically yielded $\sim$35 % larger exchange strengths than the PBE+U scheme [7]. However, as the latter might in general be less appropriate for this type of exchange coupling calculations [8], the LSDA+U scheme was chosen for the final calculations. Exchange couplings between Cu^{2+} were first calculated by assuming a pristine Li_4CuTeO_6 crystallographic structure with fully occupied Cu_2 ($2d$) and Li_3 ($4g$) sites [i.e., no minority Li^+ defects on Li_2 ($2d$) sites and no minority Cu^{2+} defects on Cu_3 ($4g$) sites]. The chosen, charge-neutral $2\times1\times2$ supercell thus contained 8 magnetic Cu_2 ions and 16 non-magnetic Li_3 ions. Out of 5 possible symmetry-distinct exchange interactions only the antiferromagnetic (AFM) exchange interaction $J_{\rm DFT} = 177.40(6)\,$K between Cu_2 sites displaced by the [101] Bravais lattice vector (i.e., in different unit cells) was found to be significant [Fig. 1(c) of the main text], with all other exchange interactions weaker than 1.5 K. The intuitive reasons for this, including nearly 90° bond angles around most O^{2-} ions (Supplementary Figure 7), are explained in the main text. The actual crystallographic structure of Li_4CuTeO_6 differs from the pristine structure in two major ways. The first is partial substitution of $1-p_2 = 7\,\%$ of magnetic Cu^{2+} by non-magnetic Li^+ on the Cu_2/Li_2 site, which breaks magnetic chains of Cu_2 sites into finite-length 1D spin chain fragments [Fig. 1(c) of the main text]. The probability of a randomly chosen Cu^{2+} on a Cu_2 site belonging to a chain fragment of length $s \geq 1$ is explicitly given by $w_2(s_2) = s_2 p_2^{s_2-1}(1-p_2)^2$ [9], which

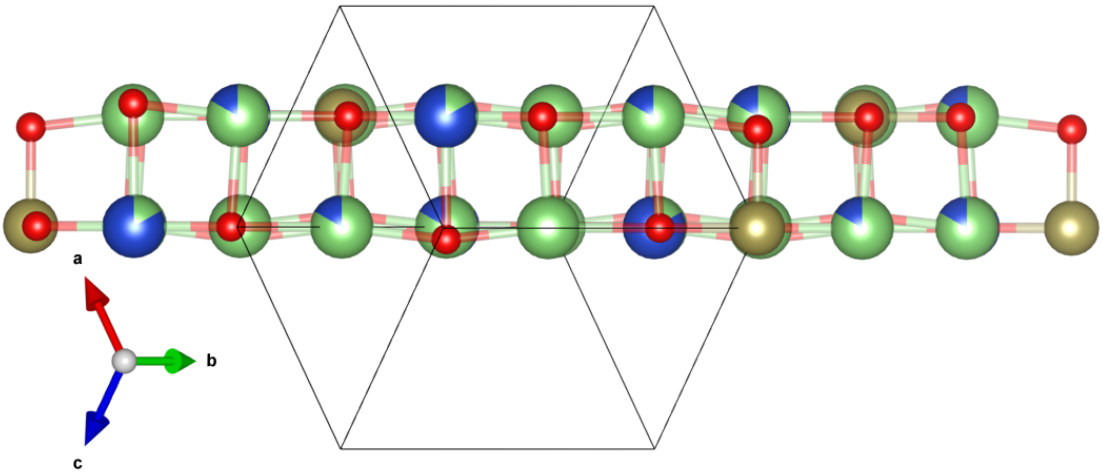

Supplementary Figure 7: Side view of a bilayer of two adjacent [101]–b planes in Li_4CuTeO_6 showing near 90° bond angles around most O^{2-} ions.

yields a mean spin chain fragment length of $S_2 = \sum_{s_2=1}^{\infty} s_2 w_2(s_2) = (1+p_2)/(1-p_2) = 11$ sites with a standard deviation of $\sqrt{S_2 - 1} = 3$.

The second major difference of the Li_4CuTeO_6 crystallographic structure from the pristine structure is the partial substitution of $p_3 = 7\,\%$ of non-magnetic Li^+ ions by magnetic Cu^{2+} ions on the Cu_3/Li_3 site. To assess the impact of this type of substitution, exchange coupling were calculated on a geometry-optimized $2 \times 1 \times 2$ supercell of pristine Li_4CuTeO_6 modified by the substitution of a single Li^+ ion by a Cu^{2+} ion on the Cu_3/Li_3 site. The electrostatic charge of the supercell was set to +1 to account for the higher oxidation number of Cu^{2+} compared to Li^+. The fitted spin model consisted of all 4 symmetry-distinct Cu_3–Cu_2 exchange couplings, as well as a single (average) Cu_2–Cu_2 exchange coupling J, as in the pristine structure. The latter simplification was needed to ensure good numerical convergence (numerical stabilization of metastable spin configurations needed to distinguish between J couplings near and far away from the Cu_3 defect was difficult), and was justified by the fact that even a free fit with all distinct J exchanges yielded at most a ±5 K variance between J near and far away from the Cu_3 defect. Out of the 4 possible Cu_3–Cu_2 couplings only the one proceeding through a nearly-linear Cu–O–Cu superexchange bridge through the $4i$ O^{2-} site yielded a huge AFM exchange coupling strength of $J'_{\mathrm{DFT}} = 824(4)$ K [Fig. 1(c) of the main text], with all other Cu_3–Cu_2 couplings being smaller than 6 K. The reasons for this are explained in the main text. We note that direct Cu_3–Cu_3 superexchange via a Cu–O–Cu

bridge (length 2.93 Å), which could potentially introduce 2D inter-chain couplings along the b axis direction (i.e., limited to a single 2D [101]–b layer; see Fig. 1(c) of the main text) and which would require more challenging LSDA+U calculations, are expected to be both very weak due to their $\approx 90°$ bond angle (Supplementary Figure 7) [10, 11], and also very rarely present due to the low probability $p_3^2 = 2.3\,\%$ of two neighboring defect Cu_3 sites being occupied at the same time. Namely, for a spin chain of length s the probability of it being isolated from all other spin chains even if strong direct Cu_3–Cu_3 exchanges were possible (and they are likely not), can be calculated to be $(1-p_3^2)^{2s_2}$; which, for a spin chain of average length $S_2 = 11$, yields a high probability of 61 % for a complete lack of this type of inter-chain coupling.

Supplementary Note 7 : Exact diagonalization calculations

A. Calculation details

Exact diagonalization (ED) calculations on the obtained J–J' spin model from DFT+U (see Fig. 1(c) of the main text) with random occupancy were performed using a custom-written parallelized sparse-matrix code for calculating thermodynamic properties (magnetic susceptibility, specific heat and entropy) of an arbitrary Heisenberg spin model with spins of arbitrary magnitude S (in the case of Li_4CuTeO_6 $S = 1/2$) in a magnetic field $\mu_0 H$ applied along the z direction, taking into account the spin-space uniaxial symmetry (conservation of the S^z total spin component) by block diagonalization of the spin Hamiltonian on distinct total S^z sectors, and time-reversal symmetry (equivalence of S^z and $-S^z$ sectors) when $\mu_0 H = 0$. The general Hamiltonian contained a Heisenberg exchange term and a Zeeman field-dependent term

$$\mathcal{H} = \sum_{\langle i,j \rangle} J_{ij} \mathbf{S}_i \cdot \mathbf{S}_j + \sum_i g_i \mu_B S_i^z \mu_0 H, \tag{2}$$

where the first sum is only over distinct pairs of spins $\langle i, j \rangle$, J_{ij} is the exchange coupling between spins $\mathbf{S}_i$ and $\mathbf{S}_j$, g_i is the g-factor of spin i (for simplicity assumed the same for all spins, $g_i = g$, in the case of Li_4CuTeO_6), and μ_B is the Bohr magneton. For a given Hamiltonian the following definitions of the molar differential magnetic susceptibility χ,

molar specific heat $C_{\rm mag}$, and molar entropy $S_{\rm mag}$ were used

$$\begin{aligned} \chi &= N_A \mu_0 \beta \left[\langle (\mu^z)^2 \rangle - \langle \mu^z \rangle^2 \right] / N, \\ C_{\rm mag} &= R \beta^2 \left[\langle \mathcal{H}^2 \rangle - \langle \mathcal{H} \rangle^2 \right] / N, \\ S_{\rm mag} &= R \left[\ln Z + \beta \langle \mathcal{H} \rangle \right] / N, \end{aligned} \tag{3}$$

where N_A is the Avogadro constant, μ_0 is the vacuum permeability, $\beta = 1/(k_B T)$ is the inverse temperature, k_B is the Boltzmann constant, $\langle A \rangle = \sum_n \langle n|A|n \rangle \, e^{-\beta E_n}/Z$ is the thermal expectation value of quantity A, $Z = \sum_n e^{-\beta E_n}$ is the partition function, E_n are the eigenenergies of the Hamiltonian $\mathcal{H}$, $R = N_A k_B$ is the gas constant, and $\mu^z = -\sum_i g_i \mu_B S_i^z$ is the z component the total magnetic moment across all spins. The special (Schottky) case of a single isolated spin ($N = 1$) is given explicitly by

$$\begin{aligned} \chi_1 &= \frac{T}{\mu_0 H^2} C_{\rm mag,1}, \\ C_{\rm mag,1} &= R \left[\left(\frac{y_0}{\sinh(y_0)} \right)^2 - \left(\frac{y_S}{\sinh(y_S)} \right)^2 \right], \\ S_{\rm mag,1} &= R \left[\ln \left(\frac{\sinh(y_S)}{\sinh(y_0)} \right) - \left(y_S \coth(y_S) - y_0 \coth(y_0) \right) \right], \end{aligned} \tag{4}$$

where $y_0 = \beta g \mu_B \mu_0 H/2$ and $y_S = (2S+1) y_0$. For low applied fields H or high T we have $\chi_1 \approx C/T$, where $C = N_A S(S+1) \mu_0 \mu_B^2 g^2/(3 k_B)$ is the molar Curie constant.

To calculate averages of thermodynamic quantities in Eq. (3) over spin-chain fragments in Li_4CuTeO_6 we first have to enumerate different possible Cu^{2+} configurations around a single spin-chain fragment and calculate the probability, that a randomly-chosen Cu^{2+} spin is part of such a configuration. Different Cu^{2+} configurations forming a single spin-chain fragment in Li_4CuTeO_6 can be succinctly indexed by specifying the vector $\mathbf{s_3} = (s_3(0), \ldots, s_3(s_2))$ containing the number $s_3(i) \in \{0, 1, 2\}$ of occupied Cu_3 sites around the i-th (if present) and $i+1$-th (if present) Cu_2 exchange bond J in a spin chain containing $s_2 \geq 1$ occupied Cu_2 sites. The total number of occupied Cu_3 sites is given by $s_3 = \sum_{i=0}^{s_2} s_3(i) \geq 0$, and the total number of Cu^{2+} ions by $N = s_2 + s_3 \geq 2$. The probability that a randomly-chosen Cu^{2+} spin is part of a spin-chain fragment given by $\mathbf{s_3}$ can be exactly calculated to be

$$w(\mathbf{s_3}) = m(\mathbf{s_3}) \frac{N}{p_2 + 2p_3} p_2^{s_2} (1-p_2)^2 p_3^{s_3} (1-p_3)^{2(s_2+1)-s_3}, \tag{5}$$

where the combinatorial multiplicity factor is given by $m(\mathbf{s_3}) = \prod_{i=0}^{s_2} \binom{2}{s_3(i)}$. The case of a

single $N = 1$ isolated Cu^{2+} ion is treated separately, where the probability that a randomly-chosen Cu^{2+} ion is isolated is given by

$$w_{\text{single}} = \alpha_2(1-p_2)^2(1-p_3)^4 + \alpha_3(1-p_2)^2, \tag{6}$$

where $\alpha_2 = p_2/(p_2+2p_3)$ is the probability that it is on a Cu_2 site and $\alpha_3 = 1-\alpha_2 = 2p_3/(p_2+2p_3)$ is the probability that it is on a Cu_3 site (note that in Li_4CuTeO_6 there are twice as many candidate Cu_3 sites than Cu_2 sites). By normalization, $w_{\text{single}} + \sum_{\mathbf{s_3}} w(\mathbf{s_3}) = 1$ where the sum is over distinct $\mathbf{s_3}$ vectors with $N \geq 2$ spins. The only remaining redundancy for $N \geq 2$ spins is given by the fact that $\mathbf{s_3} = (s_3(0), \ldots, s_3(s_2))$ and the reversed $T\mathbf{s_3} = (s_3(s_2), \ldots, s_3(0))$ vectors describe the same physical situation connected by reflection symmetry across the middle of the spin chain. Palindromic $\mathbf{s_3}$ vectors for which $\mathbf{s_3} = T\mathbf{s_3}$ are thus assigned a reflection multiplicity of $m'(\mathbf{s_3}) = 1$ and non-palindromic vectors, for which $\mathbf{s_3} \neq T\mathbf{s_3}$ are assigned a reflection multiplicity of $m'(\mathbf{s_3}) = 2$, and only one of these is considered further. Explicitly, we say that a $\mathbf{s_3}$ vector is canonical if it is either palindromic, or if the first non-zero element in $\mathbf{s_3} - T\mathbf{s_3}$ is positive. Different spin-chain fragments modulo reflection symmetry with $N \geq 2$ spins are thus uniquely indexed by canonical $\mathbf{s_3}$ vectors with $N \geq 2$, where the probability that a randomly-chosen Cu^{2+} is part of such a spin-chain fragment is given by

$$w'(\mathbf{s_3}) = m'(\mathbf{s_3})w(\mathbf{s_3}), \tag{7}$$

where $w(\mathbf{s_3})$ is given by Eq. (5), and the unique, isolated spin case $N = 1$ has probability given by Eq. (6). By normalization, $w_{\text{single}} + \sum_{\mathbf{s_3}} w'(\mathbf{s_3}) = 1$ where the sum is now over distinct canonical $\mathbf{s_3}$ vectors with $N \geq 2$ spins. To calculate averages of thermodynamic quantities in Eq. (3) over spin-chain fragments in Li_4CuTeO_6 all canonical $\mathbf{s_3}$ vectors with up to $N = 20$ spins were enumerated, their probabilities calculated using Eq. (7), and the time $t(\mathbf{s_3})$ needed to perform an ED calculation on this spin-chain fragment estimated by an empirical function $t = t(N)$. Since a permanent cache was used to avoid repeating the same calculation twice (e.g., when sweeping p_2 or p_3 probabilities), the canonical vectors already in the cache and having the same external parameters $J, J', g, \mu_0 H$ were removed from the list. From the rest a list of K_{new} canonical $\mathbf{s_3}$ vectors $\{\mathbf{s_3^{(k)}}\}_{k=1}^{K_{\text{new}}}$ with the highest estimated probability-per-calculation-time contributions to the final result, $t(\mathbf{s_3})/w'(\mathbf{s_3})$, were chosen, to ensure efficient use of computation resources. Quantities in Eq. (3) were then calculated on each chosen canonical $\mathbf{s_3}$ vector, yielding temperature dependencies $\chi^{(k)}$, $C_{\text{mag}}^{(k)}$, and $S_{\text{mag}}^{(k)}$

over the range $10\,\mathrm{mK} \leq T \leq 8000\,\mathrm{K}$ in 228 logarithmic T steps and saved to the permanent cache. To then produce the final result for a quantity $A = \chi, C_{\mathrm{mag}}, S_{\mathrm{mag}}$, the whole cache containing K canonical vectors with the same external parameters $J, J', g, \mu_0 H$ was queried for the contributions $A^{(k)}$, where $k = 1, \ldots, K$, with probabilities $w'^{(k)}$ updated to the current p_2 and p_3 using Eq. (7) and Eq. (6), and the final estimate calculated via

$$A \approx \frac{\sum_{k=1}^{K} w'^{(k)} A^{(k)}}{\sum_{k=1}^{K} w'^{(k)}}, \tag{8}$$

where the denominator is the total probability $w' = \sum_{k=1}^{K} w'^{(k)}$ contained in the K samples from the cache. In this way estimates for χ, C_{mag}, and S_{mag} temperature dependencies were calculated on $K > 13,000$ unique spin configurations with up to $N = 18$ spins and applied magnetic fields from zero to $\mu_0 H = 7\,\mathrm{T}$. Depending on the chosen external parameters and p_2 and p_3, total probabilities in excess of $w' > 98.8\,\%$ could be reached in favorable, and $w' > 60.2\,\%$ in unfavorable, cases.

Finally, we note that to convert between ED quantities calculated via Eq. (8), which are given per mole of actual Cu^{2+} in $Li_{6-2x}Cu_xTeO_6$, and experimental measurements, which are given per mole of ideal formula unit Li_4CuTeO_6, we have to multiply all raw ED data by a factor $x = p_2 + 2p_3$, i.e., by the average number of Cu^{2+} ions per actual formula unit.

B. Results

Supplementary Figure 8 shows the ED calculated T-dependent molar susceptibility in zero field for the (high-T) spin model of Li_4CuTeO_6 from DFT at parameters extracted from experiment (see ED fits in the main text), but allowing for Cu_3 occupancy probability p_3 to vary. In the $p_3 = 0$ case, which corresponds to pure random-length Cu_2 spin chains with exchange J with no Cu_3 spins around them, we see a broad shoulder starting to develop around $T \sim J = 244\,\mathrm{K}$ and persisting down to $T \sim 0.14J = 35\,\mathrm{K}$ where the susceptibility becomes almost T-independent due to gradual freezing out of internal spin-chain fragment spin degrees of freedom. Below $T \sim 0.1J = 24\,\mathrm{K}$ we enter the regime of seemingly quasi-free spins a Curie-like behavior, which arises mainly from spin-chain fragments with an odd number of spins $N \geq 3$, whose total spin cannot be lower than $1/2$ by the rules for quantum addition of spin and thus behave as discrete units with finite effective spin, in addition to the fraction w_{single} of isolated ($N = 1$) truly free spins. As the occupancy p_3 of Cu_3 sites is

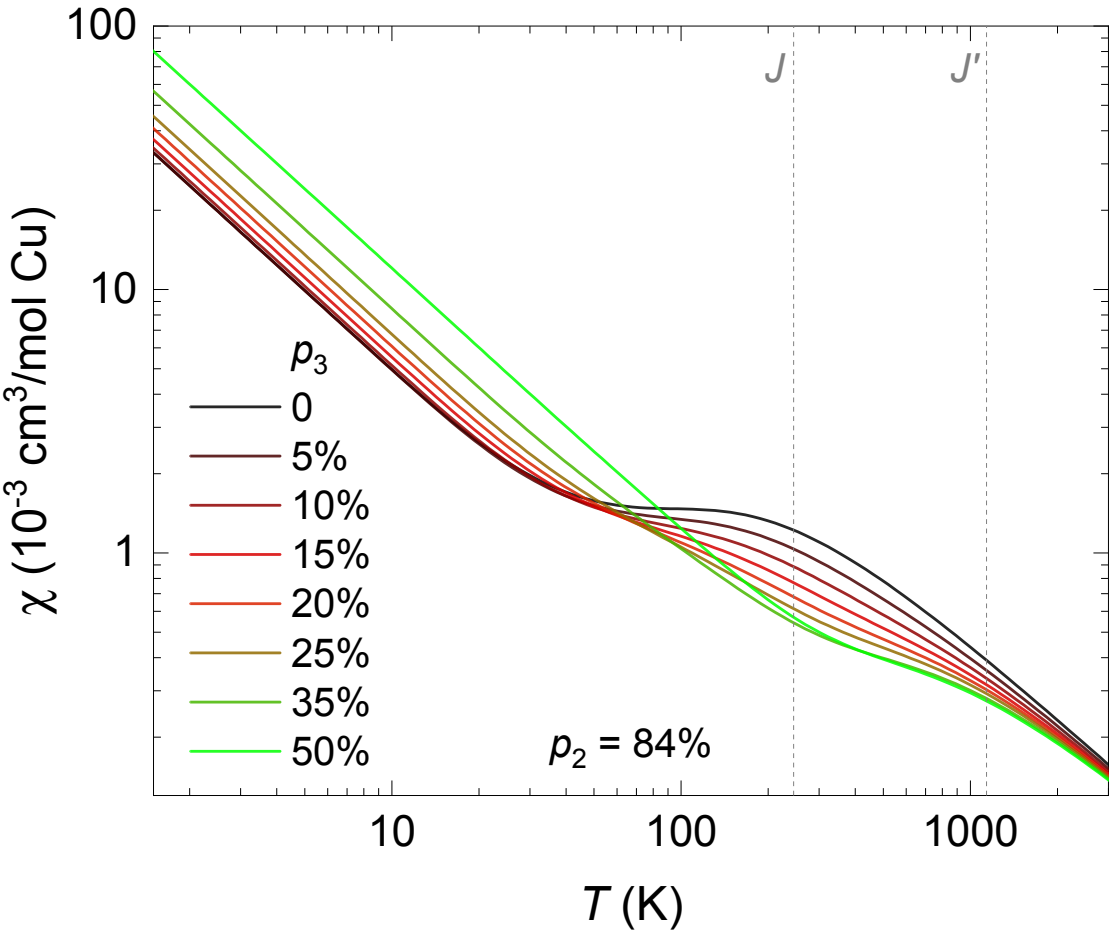

Supplementary Figure 8: ED calculated susceptibility of the high-T spin model of Li_4CuTeO_6 at the experimental Cu_2 occupancy probability $p_2 = 84\,\%$, spin-chain exchanges $J = 244\,\mathrm{K}$ and $J' = 1140\,\mathrm{K}$, and Cu^{2+} $g = 2.28$ (see main text) for a range of Cu_3 occupancy probabilities p_3. This raw ED data was not multiplied by the conversion factor $x = p_2 + 2p_3$ for comparison with experiment.

increased, the $T \sim J$ shoulder is smoothed out and gradually shifted to higher T while a new shoulder starts emerging at $T \sim J'$, where above the shoulder, $T \gg J' = 1140\,\mathrm{K}$, all Cu^{2+} spins are in the paramagnetic Curie–Weiss regime, while below it, $T < J'$, spins on Cu_3 sites start forming strongly-bound singlets (if bound to a single Cu_2 spin) or triplets (if bound to two Cu_2 spins) due to strong Cu_3–Cu_2 bonds J'. When $p_3 > 0$ the high-T Curie–Weiss limit would thus only be reached at extremely high $T \gg J'$. In Supplementary Figure 9 the ED calculated molar specific heat is compared with experimental total specific heat data in a range of applied magnetic fields $\mu_0 H$. Like in experiment, a specific heat peak

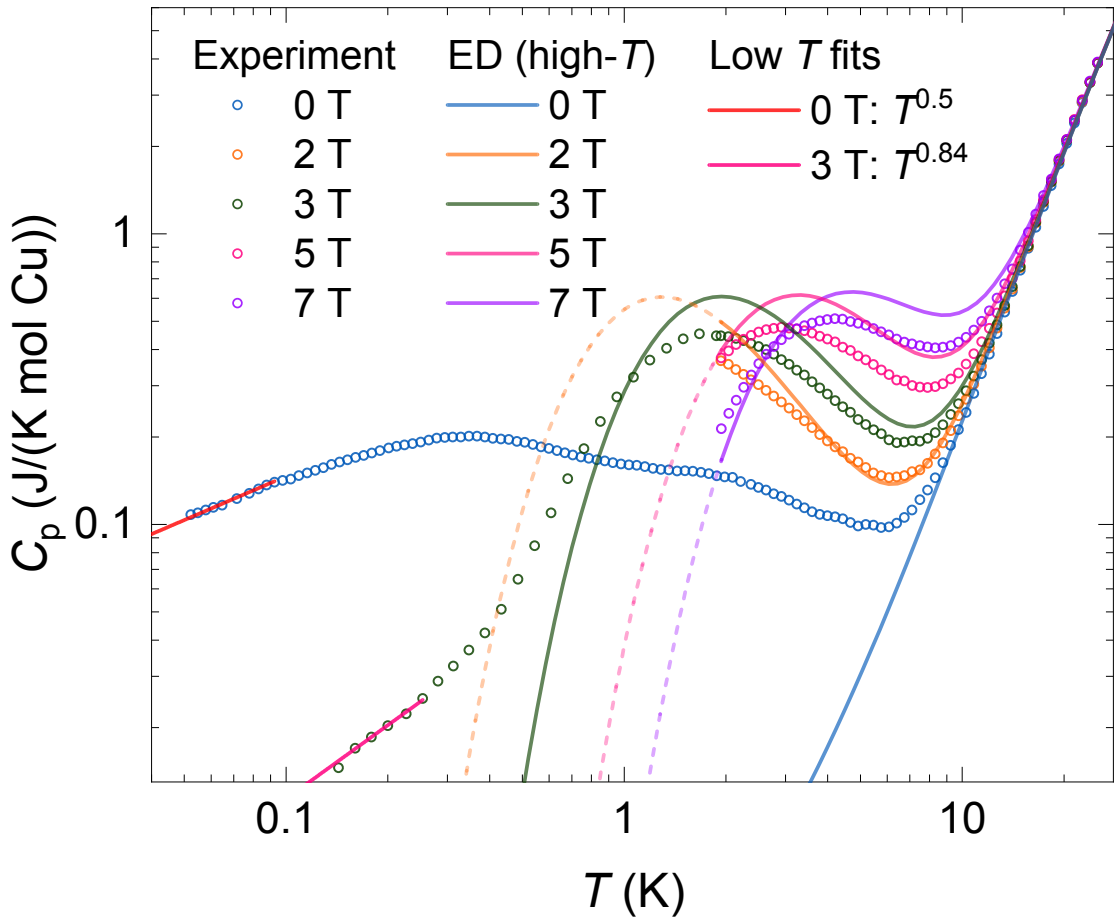

Supplementary Figure 9: Comparison of experimental total specific heat (symbols) with the ED-calculated specific heat (lines) of the high-T spin model of Li_4CuTeO_6 at the experimental Cu_2 occupancy probability $p_2 = 84\,\%$, spin-chain exchanges $J = 244\,\mathrm{K}$ and $J' = 1140\,\mathrm{K}$, Cu^{2+} $g = 2.28$, and susceptibility-fitted $p_3 = 20\,\%$ (see main text) in a range of applied fields $\mu_0 H$. A simplified Debye contribution $\propto T^3$ was added to the ED calculation to describe the lattice contribution to the experimentally observed specific heat, and the raw ED data was multiplied by the conversion factor $x = p_2 + 2p_3$ for comparison with experiment. Also shown are very-low-T power-law fits of the experimental specific heat data in 0 and 3 T.

appears at low-T in non-zero applied fields in the ED calculations and at a position that scales with H due to the opening of a Zeeman energy gap of both isolated ($N = 1$) spins and spin-chain fragments with an odd number of spins $N \geq 3$ with a ground state spin $\geq 1/2$. However, in contrast to ED calculations, a lot of experimental low-T specific heat intensity in Li_4CuTeO_6 is shifted to much lower T in non-zero applied fields due to additional frustrated

inter-chain couplings J_{inter} (see main text), which results in a suppression of the specific heat peak height and the appearance of a long power-law tail at the lowest T instead of gapped behavior expected from the high-T model high-T spin model of Li_4CuTeO_6 from DFT where $J_{\text{inter}} = 0$ is implicitly assumed. This is another robust indication of strong antiferromagnetic frustration and a nearly-degenerate ground state in this compound. Furthermore, the effect is even stronger in zero applied field, where ED calculated specific heat quickly tends to zero below $\sim$10 K, while the experimental specific heat exhibits a very broad response with a local peak around 0.4 K, and power-law behavior at the lowest T. This indicates the gradual release of $S_{\text{mag}}(0) = 13.5\,\%R\ln 2$ residual entropy predicted ED calculations on the high-T model without inter-chain couplings in zero field at $T \ll J, J'$. This residual entropy arises almost exclusively (to within $\approx$1 %) due to ground-state degeneracy of both isolated ($N = 1$) spins (double ground state degeneracy accounting for $10.8\,\%R\ln 2$ of residual entropy per mole of actual Cu^{2+}), as well as finite- (mostly odd-) length spin-chain fragments with $N \geq 2$ (accounting for $2.7\,\%R\ln 2$ of residual entropy) in zero field due to time-reversal symmetry (Kramers degeneracy), which cannot be lifted by two-spin interactions. An applied magnetic field can lift this Kramers degeneracy by breaking time-reversal symmetry (leading to a $\mu_0 H$-dependent specific heat peak discussed above), while inter-chain couplings can cause a release of this local excess entropy by coupling the spin-chain fragments together into a larger random spin lattice (lifting the degeneracy of individual spin-chain fragments by hybridization), as is the case in Li_4CuTeO_6. No other substantial ground-state degeneracy of isolated spin-chain fragments is detected by ED ($<1\,\%R\ln 2$ entropy), meaning that in zero field the huge release of $\sim 13\,\%R\ln 2$ entropy around 0.4 K in Li_4CuTeO_6 can only be explained by the lifting of extensive Kramers degeneracy due to inter-chain couplings, and not by any perturbations within individual, isolated spin-chain fragments (e.g., magnetic anisotropy). Both non-zero and zero-applied field specific heat data when compared with ED calculations thus clearly show the crucial impact of frustrated inter-chain couplings on the thermodynamics behavior of Li_4CuTeO_6 at low-T.

Supplementary References

[1] S. Kundu, A. Shahee, A. Chakraborty, K. M. Ranjith, B. Koo, J. Sichelschmidt, M. T. F. Telling, P. K. Biswas, M. Baenitz, I. Dasgupta, S. Pujari, and A. V. Mahajan, Phys. Rev. Lett. **125**, 267202 (2020).

[2] S. J. Clark, M. D. Segall, C. J. Pickard, P. J. Hasnip, M. J. Probert, K. Refson, and M. Payne, Z. Kristall. **220**, 567 (2005).

[3] V. I. Anisimov, F. Aryasetiawan, and A. I. Lichtenstein, J. Phys.: Condens. Matter **9**, 767 (1997).

[4] D. Wang, X. Bo, F. Tang, and X. Wan, Phys. Rev. B **99**, 035160 (2019).

[5] H. J. Monkhorst and J. D. Pack, Phys. Rev. B **13**, 5188 (1976).

[6] K. Riedl, Y. Li, R. Valentí, and S. M. Winter, Phys. Status Solidi (B): Basic Res. **256**, 1800684 (2019).

[7] J. P. Perdew, K. Burke, and M. Ernzerhof, Phys. Rev. Lett. **77**, 3865 (1996).

[8] S. Sharma, E. K. U. Gross, A. Sanna, and J. K. Dewhurst, J. Chem. Theory Comput. **14**, 1247 (2018).

[9] D. Stauffer, *Introduction to percolation theory* (Taylor & Francis, London Bristol, Pennsylvania, 1994).

[10] J. Goodenough, *Magnetism and the chemical bond* (R.E. Krieger Pub. Co, Huntington, N.Y, 1976).

[11] X. Rocquefelte, K. Schwarz, and P. Blaha, Sci. Rep. **2**, 1 (2012).